

# Microchannel Simulation

Mohammad Hassan Saidi, Omid Asgari and Hadis Hemati  
*Sharif University of Technology*  
*Iran*

## 1. Introduction

In the current state of fast developing electronic equipment, having high speeds and at the same time high heat generation rates, researchers are trying to find an effective microcooling method. The main problem in the cooling of microdevices is their high heat generation rate in a limited space. In this way, much research has been conducted on the analysis of different novel microcooling methods such as microheat pipes, microjet impingements, microcapillary pumped loops, microelectrohydrodynamic coolers, and microchannel heat sinks. Among the different microcooling devices the microchannel heat sink has been of special consideration due to its capabilities such as high capacity of heat removal. In principle, microchannels can be machined at the back of a substrate of electronic chips and, therefore, can reduce the internal (contact) thermal resistance of the heat sink practically to zero. The cooling rates in such microchannel heat exchangers should increase significantly due to a decrease in the convective resistance to heat transport caused by a drastic reduction in the thickness of thermal boundary layers.

The overall excellent potential capacity of such a heat sink for heat dissipation is based on the large heat transfer surface-to-volume ratio of the microchannel heat exchangers. The use of microchannel heat sink was first introduced by Tuckerman and Pease in 1981 [1]. Their research was based on an experiment where they showed that high heat rates of  $790 \text{ W/cm}^2$  could be removed by microchannel heat sinks.

Currently, research in the field of microchannels is going on in three aspects of experimental methods [2,3,4], numerical methods [5,6,7,8], and analytical methods [9,10,11,12]. It is well known that the cross-sectional shape of a channel can have significant affect on the fluid flow and heat transfer characteristics in microchannels. Peng and Peterson [13] performed experimental investigations of the pressure drop and convective heat transfer for water flowing in rectangular microchannels, and found that the cross-sectional aspect ratio had significant influence on the flow friction and convective heat transfer in both laminar and turbulent flows. Kawano et al. [14] provided experimental data on the friction and heat transfer in rectangular, silicon based microchannel heat sinks, and more recently Wu and Cheng [15,16] conducted a series of experiments to measure the friction factor and convective heat transfer in smooth silicon microchannels of trapezoidal cross-section. The experimental methods has its own values and the new developments in the micromachining techniques help the researchers to perform precise experiments, but because of its high cost it fails to be commonly applied.

There has been much effort to analytically model the microchannel heat sink. Knight et al. [9] used empirical correlations to evaluate the performance of a microchannel heat sink. Koh and Colony [17] first modeled microstructures as a porous medium using Darcy's law. Later on Tien and Kuo [18] developed a model for heat transfer in microchannels using the modified Darcy equation and the two-equation model. Another method to model the microchannel heat sink analytically is to use the fin and plate theory. In this way, the solid walls are assumed to be as fins that are connected to the base plate. Applying this assumption, the thermal resistance and other thermal characteristics of the system could be derived using the fin and plate heat transfer relations. Because of limiting and less accuracy of the analytical approach in some phenomena, e.g. conjugate heat transfer the numerical method is being used vastly to simulate the performance of microchannels like other fields of heat transfer.

Webb and Zhang [19] claim that the accepted single-phase flow correlations adequately predict their experimental data for round and rectangular tubes with hydraulic diameter of the order of 1 mm. Wesberg et al. [8] solved a two-dimensional conjugate heat transfer problem for microchannel heat sinks to obtain detailed spatial distributions of the temperature of the heat sink cross-section along the length of the channels. Fedorov and Viskanta [6] developed a three dimensional model to investigate the conjugate heat transfer in a microchannel heat sink with the same channel geometry used in the experimental work done by Kawano et al. [14]. This simulation showed that the average channel wall temperature along the flow direction was nearly uniform except in the region close to the channel inlet, where very large temperature gradients were observed. Qu and Mudawar [5] conducted a three-dimensional fluid flow and heat transfer analysis for a rectangular microchannel heat sink with a geometry similar to that of Kawano et al. [14] using a numerical method similar to that proposed by both Kawano et al. [14] and Fedorov and Viskanta [6]. This model considered the hydrodynamic and thermal developing flow along the channel and found that the Reynolds number will influence the length of the developing flow region. It was also found that the highest temperature is typically encountered at the heated base surface of the heat sink immediately adjacent to the channel outlet and that the temperature rise along the flow direction in the solid and fluid regions can both be approximated as linear.

In this study the SIMPLE pressure correction approach has been chosen. For simplicity the equations are solved in a segregated manner. An effective multigrid solver is developed for pressure correction equation. Methods for calculating cell-face velocities are studied. Convection and diffusion terms are modeled using upwind and the central difference stencil, respectively. The variables are located in the cell-centred colocated grid. The general coordinates are described using the pure control volume approach with vector notations. In the method developed herein, the velocity field is first solved and then the mean velocity derived. The thermophysical properties are chosen at a reference temperature (an estimated averaged liquid bulk temperature) determined from the energy balance and then a new final velocity field and temperature distribution for the microchannel is defined. A numerical model with fully developed flow is presented and used to analyze the heat transfer in a microchannel heat sink for low Re numbers. The numerical model is based upon a three dimensional conjugate heat transfer approach (3D fluid flow and 3D heat transfer). Computations were performed for different total pressure drops in the channel. The system of three-dimensional Navier-Stokes equations for conservation of mass, momentum, and energy based on the continuum flow assumption is used as a mathematical model of the process.

## 2. Analysis

### 2.1 Problem description

The micro-heat sink modeled in this investigation consists of a 10 mm long silicon substrate with a silicon cover. The rectangular microchannels have a width of  $57 \mu\text{m}$  and a depth of  $180 \mu\text{m}$ . The hydraulic diameter of microchannel under development is about  $86.58 \mu\text{m}$  and is expected to decrease to  $10 \mu\text{m}$ . This yields a typical Knudsen number for water as a coolant to be between  $3.5 \times 10^{-5}$  and  $3.5 \times 10^{-4}$  which lies in the continuous flow regime ( $Kn < 10^{-3}$ ) [20]. Hence, the conservation equations based on the continuum model (Navier-Stokes equations of motion) can still be used to describe the transport processes.

A schematic of the rectangular microchannel heat sink is shown in Figure 1 where a unit of cell consisting of one channel was selected because of the symmetry of the structure. The unit cell of the heat sink can be represented by an asymmetric rectangular channel with the cross-sectional dimensions as shown in Table 1. The channel geometry is similar to that employed in the experimental work of Kawano et al. [14] and in the numerical investigations of Qu and Mudawar [5] and Fedorov and Viskanta [6]. It is assumed that the heat flux input at the bottom of the heat sink is uniform.

### 2.2 Model equations and boundary conditions

Consider a steady 3D flow in a silicon microchannel heat sink with heating from below and with adiabatic conditions at the other boundaries, as showed in Figure 1. There are some assumptions in this numerical simulation, e.g. the transport processes are considered to be steady-state and three-dimensional, the flow is incompressible and laminar, thermal radiation is neglected, the thermophysical properties are temperature dependent. Under the stated assumptions, the governing equations and related boundary conditions for a fully developed 3D flow heat transfer are given as [21],

- Continuity equation

$$\frac{\partial}{\partial x}(\rho u) + \frac{\partial}{\partial y}(\rho v) + \frac{\partial}{\partial z}(\rho w) = 0 \quad (1)$$

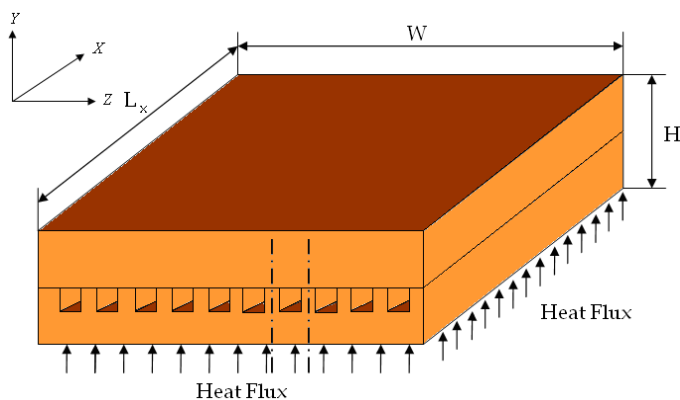


Fig. 1. Part I

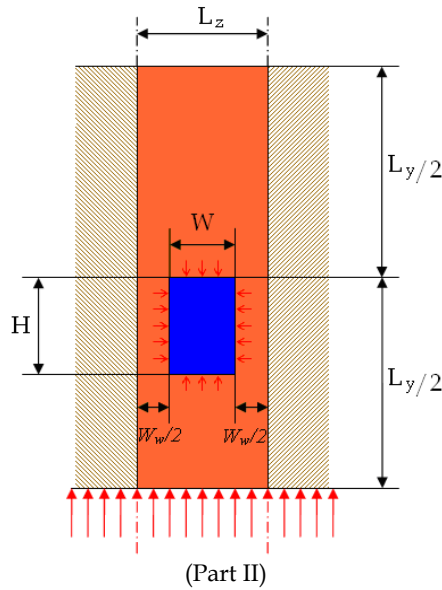


Fig. 1. Schematic of a rectangle microchannel heat sink and the unit cell.

$H$ $\mu m$	$L_x$ $\mu m$	$L_z$ $\mu m$	$L_y$ $\mu m$	$D_h$ $\mu m$	$W_w$ $\mu m$	$W$ $\mu m$
180	10	100	900	86.58	43	57

Table 1. Geometric dimensions of the unit cell.

- Momentum equations

$$\begin{aligned} & \frac{\partial}{\partial x}(\rho u^2) + \frac{\partial}{\partial y}(\rho uv) + \frac{\partial}{\partial z}(\rho uw) \\ &= -\frac{\partial P}{\partial x} + \frac{\partial}{\partial x}\left(\mu \frac{\partial u}{\partial x}\right) + \frac{\partial}{\partial y}\left(\mu \frac{\partial u}{\partial y}\right) + \frac{\partial}{\partial z}\left(\mu \frac{\partial u}{\partial z}\right) \end{aligned} \tag{2}$$

$$\begin{aligned} & \frac{\partial}{\partial x}(\rho uv) + \frac{\partial}{\partial y}(\rho v^2) + \frac{\partial}{\partial z}(\rho vw) \\ &= -\frac{\partial P}{\partial y} + \frac{\partial}{\partial x}\left(\mu \frac{\partial v}{\partial x}\right) + \frac{\partial}{\partial y}\left(\mu \frac{\partial v}{\partial y}\right) + \frac{\partial}{\partial z}\left(\mu \frac{\partial v}{\partial z}\right) \end{aligned} \tag{3}$$

$$\begin{aligned} & \frac{\partial}{\partial x}(\rho wu) + \frac{\partial}{\partial y}(\rho wv) + \frac{\partial}{\partial z}(\rho w^2) \\ &= -\frac{\partial P}{\partial z} + \frac{\partial}{\partial x}\left(\mu \frac{\partial w}{\partial x}\right) + \frac{\partial}{\partial y}\left(\mu \frac{\partial w}{\partial y}\right) + \frac{\partial}{\partial z}\left(\mu \frac{\partial w}{\partial z}\right) \end{aligned} \tag{4}$$

- Energy equation

$$\begin{aligned} & \frac{\partial}{\partial x}(c_p \rho u T) + \frac{\partial}{\partial y}(c_p \rho v T) + \frac{\partial}{\partial z}(c_p \rho w T) \\ &= \frac{\partial}{\partial x}\left(k \frac{\partial T}{\partial x}\right) + \frac{\partial}{\partial y}\left(k \frac{\partial T}{\partial y}\right) + \frac{\partial}{\partial z}\left(k \frac{\partial T}{\partial z}\right) \end{aligned} \tag{5}$$

where  $u, v, w, p, \rho, \mu, T, k$  and  $c_p$  are the velocity in  $x$ -direction,  $y$ -direction,  $z$ -direction, pressure, density, dynamic viscosity, temperature, thermal conductivity and specific heat at constant pressure respectively. The hydrodynamic boundary conditions are as follow:

at the inner wall surface (no slip)

$$u = 0, \quad v = 0, \quad w = 0 \tag{6}$$

at the inlet of channel

$$x = 0, \quad p_f = p_{in}, \quad u = 1 \frac{m}{s}, \quad v = 0, \quad w = 0 \tag{7}$$

at the outlet of channel

$$x = L_x, \quad p_f = p_{out}(1atm), \quad v = 0, \quad w = 0 \tag{8}$$

the heat conduction in the solid section is,

$$\frac{\partial}{\partial x}\left(k \frac{\partial T}{\partial x}\right)_s + \frac{\partial}{\partial y}\left(k \frac{\partial T}{\partial y}\right)_s + \frac{\partial}{\partial z}\left(k \frac{\partial T}{\partial z}\right)_s = 0 \tag{9}$$

the thermal boundary conditions can be stated as:

$$0 \leq x \leq L_x, y = 0, 0 \leq z \leq L_z \Rightarrow -k_s \frac{\partial T_s}{\partial y} = q_s \tag{10}$$

$$0 \leq x \leq L_x, y = L_y, 0 \leq z \leq L_z \Rightarrow -k_s \frac{\partial T_s}{\partial y} = 0 \tag{11}$$

$$\begin{aligned} x = 0 \left\{ \begin{array}{l} (L_y / 2 - H) \leq y \leq L_y / 2 \\ W_w / 2 \leq z \leq (W_w / 2 + W) \end{array} \right. & \Rightarrow T_f = T_{in} \\ \text{else} & \Rightarrow -k_s \frac{\partial T_s}{\partial x} = 0 \end{aligned} \tag{12}$$

$$\begin{aligned} x = L_x \left\{ \begin{array}{l} (L_y / 2 - H) \leq y \leq L_y / 2 \\ W_w / 2 \leq z \leq (W_w / 2 + W) \end{array} \right. & \Rightarrow -k_f \frac{\partial T_f}{\partial x} = 0 \\ \text{else} & \Rightarrow -k_s \frac{\partial T_s}{\partial x} = 0 \end{aligned} \tag{13}$$

$$0 \leq x \leq L_x, 0 \leq y \leq L_y, z = 0 \Rightarrow -k_s \frac{\partial T_s}{\partial z} = 0 \quad (14)$$

$$0 \leq x \leq L_x, 0 \leq y \leq L_y, z = L_z \Rightarrow -k_s \frac{\partial T_s}{\partial z} = 0 \quad (15)$$

at the inner wall surface,

$$\begin{aligned} -k_s \left( \frac{\partial T_s(x, y, z)}{\partial n} \Big|_{\Gamma} \right) &= -k_f \left( \frac{\partial T_f(x, y, z)}{\partial n} \Big|_{\Gamma} \right) \\ T_{s,\Gamma} &= T_{f,\Gamma} \end{aligned} \quad (16)$$

where, Equation (10) gives the uniform heat flux boundary condition at the bottom wall of the substrate. Equations (11)–(15) assumes no heat loss from the solid to the environment at the boundary except at  $x = 0$  for the fluid, where  $T_f = T_{in}$ . It should be noted that in reality, heat losses from the heat sink to the environment should be considered by conduction and convection at the inlet and outlet and at the top surface of the heat sink. Heat transfer in the unit cell is a conjugate one combining heat conduction in the solid and convection to the cooling fluid. The two heat transfer modes are coupled by continuities of temperature and heat flux at the interface between the solid and fluid, which are expressed by Equation (16).  $\Gamma$  denotes the perimeter of the inner wall of the channel. Equations (1), (2), (3), (4) and (5) form a closed system from which the flow properties  $u$ ,  $v$ ,  $w$ ,  $p$  and  $T$  can be solved as a function of space and time. But, in this study only steady-state flows will be calculated.

### 2.3 Calculation of incompressible flows

Simultaneous numerical calculation of Equations (1), (2), (3), (4) and (5) is computationally complex. Therefore, the equations are solved one after another, i.e. in a segregated manner. The basic structure of Equations (2), (3), (4) and (5) is similar to each other, containing an unsteady term, convection, diffusion and possibly source terms, and they are often called convection-diffusion equations. The flow properties  $u$ ,  $v$ ,  $w$  and  $T$  are solved from Equations (2), (3), (4) and (5) respectively. Therefore, the continuity Equation (1) is to be modified for pressure or pressure-like quantity. The first stage is to derive a convection-diffusion equation to finite form. In this study the control volume approach is utilized. The process is to be studied by the aid of a general convection-diffusion equation for quantity  $\Phi$ ,

$$\begin{aligned} \frac{\partial}{\partial x}(\rho u \phi) + \frac{\partial}{\partial y}(\rho v \phi) + \frac{\partial}{\partial z}(\rho w \phi) \\ = \frac{\partial}{\partial x} \left( \alpha \frac{\partial \phi}{\partial x} \right) + \frac{\partial}{\partial y} \left( \alpha \frac{\partial \phi}{\partial y} \right) + \frac{\partial}{\partial z} \left( \alpha \frac{\partial \phi}{\partial z} \right) + S \end{aligned} \quad (17)$$

where  $\alpha$  is diffusion coefficient and the source term  $S$  could contain, for instance, pressure gradient and/or body force, etc. Next, Equation (17) is integrated over the control volume  $V_{i,j,k}$ . After the rearrangements the integrated equation can be obtained in the form,

$$\begin{aligned}
 &F_{i+1/2,j,k} - F_{i-1/2,j,k} + F_{i,j+1/2,k} - \\
 &F_{i,j-1/2,k} + F_{i,j,k+1/2} - F_{i,j,k-1/2} = S_{i,j,k}
 \end{aligned}
 \tag{18}$$

$$F_{i-1/2,j,k} = \left[ A \left( \rho u \phi - \alpha \frac{\partial \phi}{\partial x} \right) \right]_{i-1/2,j,k}
 \tag{19}$$

where  $A$  is a surface area of a face of the cell. From the physical point of view, the convection transfers the information downstream. Therefore, the approximation of convection terms must be weighted to the up-stream-side. The simplest stencil is the first-order upwind (FOU),

$$\phi_{i-1/2,j,k} = \phi_{i-1,j,k} + O(\Delta x); \quad u_{i-1/2,j,k} > 0
 \tag{20}$$

$$\phi_{i-1/2,j,k} = \phi_{i,j,k} + O(\Delta x); \quad u_{i-1/2,j,k} < 0
 \tag{21}$$

The diffusion terms of Equation (19) are approximated by using the central difference scheme,

$$\left[ \frac{\partial \phi}{\partial x} \right]_{i+1/2,j,k} = \frac{\phi_{i+1,j,k} - \phi_{i,j,k}}{\Delta x} + O(\Delta x^2)
 \tag{22}$$

where the grid is assumed to be uniform. Also the pressure gradient terms of the momentum equations are approximated by using central differencing. After the integration over the control volume  $V_{i,j,k}$  they are obtained in the form

$$\int_{V_{i,j,k}} \frac{\partial p}{\partial x} d\Omega = (pA)_{i+1/2,j,k} - (pA)_{i-1/2,j,k}
 \tag{23}$$

where central difference schemes like,

$$p_{i+1/2,j,k} = 0.5(p_{i,j,k} + p_{i+1,j,k}) + O(\Delta x^2)
 \tag{24}$$

are applied.

To close the partial differential equation system (1), (2), (3), (4) and (5) for a certain problem, the boundary conditions must be specified. In the present solver, the boundary conditions are handled by using ghost cells, which are illustrated in Figures (2) and (3), the principal idea is to use the ghost cell values to give the fixed boundary value at the boundary of the domain, i.e. the ghost cell values are extrapolated from the face and domain values. Thus, the Dirichlet and Neumann conditions are given in the form

$$\phi_{2,j,k} = 2\phi_{face} - \phi_{3,j,k}
 \tag{25}$$

$$\phi_{2,j,k} = \phi_{3,j,k} - \Delta x \left. \frac{\partial \phi}{\partial x} \right|_{face}
 \tag{26}$$

respectively.

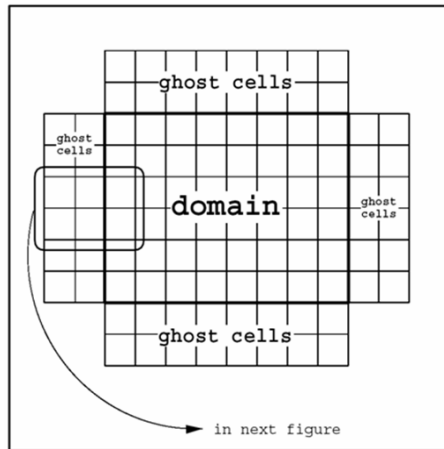


Fig. 2. Ghost cells around the domain.

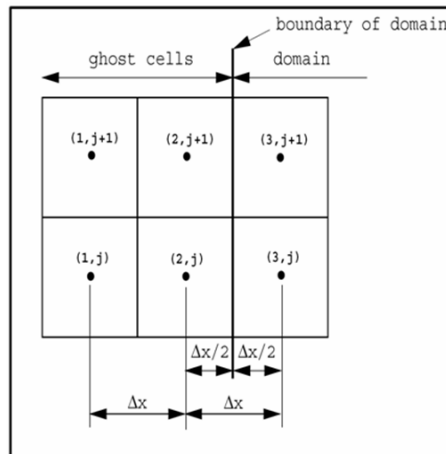


Fig. 3. The notations of the ghost cells.

## 2.4 Treatment of pressure in incompressible Navier-Stokes equations

The spatial oscillations occur when central differencing is applied to both the continuity equation and the pressure gradient term in the momentum equations. The momentum equations at the even-numbered nodes depend only on pressures at odd-numbered nodes, and vice versa. The same holds for the continuity equation. This situation permits two different pressure fields to co-exist, which is known as checkerboard pressure field.

Nowadays, the staggered grid arrangement is no more necessary. The remarkable turn toward the collocated grid arrangement was the study presented by Rhie and Chow [22]. In the collocated grid arrangement all variables use the same grid and interpolation is needed. As it was mentioned, the collocated grid arrangement causes problems when central

differencing is applied to cell-face velocities, Rhie and Chow [21] presented a method for avoiding the usage of the staggered grid arrangement. In this method central differencing has been applied to the pressure gradient and cell-face pressure, while the Rhie & Chow interpolation has been applied to the cell-face velocity as follow,

$$u_{i-1/2,j,k} = \frac{1}{2}(u_{i-1,j,k} - u_{i,j,k}) - \frac{1}{2} \left( \frac{V_{i-1,j,k}}{a_{i-1,j,k}} + \frac{V_{i,j,k}}{a_{i,j,k}} \right) \times \frac{\partial p}{\partial x} \Big|_{i-1/2,j,k} + \frac{1}{2} \left( \frac{V_{i-1,j,k}}{a_{i-1,j,k}} \frac{\partial p}{\partial x} \Big|_{i-1,j,k} + \frac{V_{i,j,k}}{a_{i,j,k}} \frac{\partial p}{\partial x} \Big|_{i,j,k} \right) \tag{27}$$

**2.5 Pressure correction equation and multigrid technique**

The current research indicates that the AC-MG acceleration technique is highly efficient, reliable and robust, which makes it feasible for CPU-intensive computations, such as pressure Correction equations. When compared to the discretized momentum equations, the pressure Poisson equations tend to be very stiff and ill-conditioned, i.e.  $a_p \equiv \sum_{nb} a_{nb}$  because of these reasons, solving the pressure Poisson equation is usually the CPU bottle-neck for the incompressible N-S equation system and AC-MG technique is required. With this acceleration technique the residuals of the large-scale algebraic equation system are guaranteed to be continuously driven down to the level of the computer machine round-off error and warrants strong conservations of mass and momentum satisfied over all the control volumes. In this cell centered multigrid algorithm both restriction and prolongation operators are based on piecewise constant interpolation.

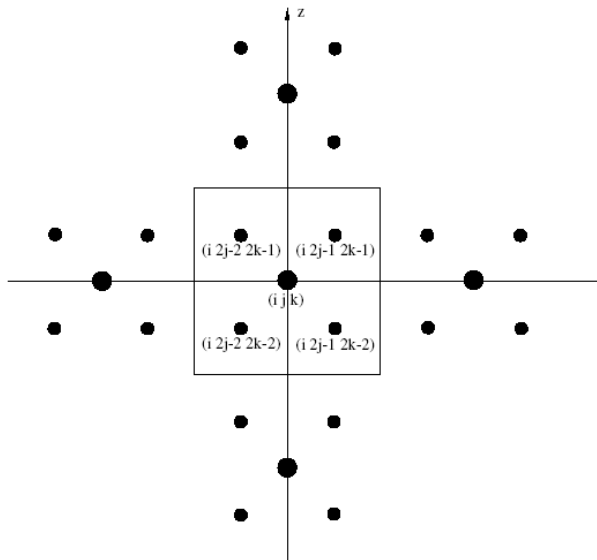


Fig. 4. Schematic of a cell-centered two-level multigrid configuration.

The additive-correction multigrid scheme described in [23] is used for the two cross-streamwise directions ( $y$  and  $z$ ). The cell-centred two-level multigrid configuration is sketched in Figure 4, in which the grid point  $(i, j, k)$  on the coarse level is surrounded by four grid points on the fine level in the  $y$  and  $z$  directions, namely  $(i, 2j-2, 2k-2)$ ,  $(i, 2j-2, 2k-1)$ ,  $(i, 2j-1, 2k-2)$  and  $(i, 2j-1, 2k-1)$ . The variables on the coarse and fine levels are denoted by superscripts  $c$  and  $f$ , respectively, in the following equations. Based on the idea introduced in [23], the following algebraic equation system can be used to determine the correction for the fine grid level:

$$\begin{aligned} a_{p(i,j,k)}^c \phi_{i,j,k}^c &= a_{e(i,j,k)}^c \phi_{i+1,j,k}^c + a_{w(i,j,k)}^c \phi_{i-1,j,k}^c \\ &+ a_{n(i,j,k)}^c \phi_{i,j+1,k}^c + a_{s(i,j,k)}^c \phi_{i,j-1,k}^c \\ &+ a_{t(i,j,k)}^c \phi_{i,j,k+1}^c + a_{b(i,j,k)}^c \phi_{i,j,k-1}^c + S c_{i,j,k}^c \end{aligned} \quad (28)$$

where the coefficients on the coarse grid are calculated from the following restriction formulae:

$$\begin{aligned} a_{e(i,j,k)}^c &= a_{e(i,2j-2,2k-2)}^f + a_{e(i,2j-2,2k-1)}^f \\ &+ a_{e(i,2j-1,2k-2)}^f + a_{e(i,2j-1,2k-1)}^f \end{aligned} \quad (29)$$

$$\begin{aligned} a_{w(i,j,k)}^c &= a_{w(i,2j-2,2k-2)}^f + a_{w(i,2j-2,2k-1)}^f \\ &+ a_{w(i,2j-1,2k-2)}^f + a_{w(i,2j-1,2k-1)}^f \end{aligned} \quad (30)$$

$$a_{n(i,j,k)}^c = a_{n(i,2j-1,2k-2)}^f + a_{n(i,2j-1,2k-1)}^f \quad (31)$$

$$a_{s(i,j,k)}^c = a_{s(i,2j-2,2k-2)}^f + a_{s(i,2j-2,2k-1)}^f \quad (32)$$

$$a_{t(i,j,k)}^c = a_{t(i,2j-2,2k-1)}^f + a_{t(i,2j-1,2k-1)}^f \quad (33)$$

$$a_{b(i,j,k)}^c = a_{b(i,2j-2,2k-2)}^f + a_{b(i,2j-1,2k-2)}^f \quad (34)$$

$$\begin{aligned} a_{p(i,j,k)}^c &= a_{p(i,2j-2,2k-2)}^f + a_{p(i,2j-2,2k-1)}^f \\ &+ a_{p(i,2j-1,2k-2)}^f + a_{p(i,2j-1,2k-1)}^f \\ &- a_{s(i,2j-1,2k-2)}^f + a_{s(i,2j-1,2k-1)}^f \\ &- a_{n(i,2j-2,2k-2)}^f + a_{n(i,2j-2,2k-1)}^f \\ &- a_{b(i,2j-2,2k-1)}^f + a_{b(i,2j-1,2k-1)}^f \\ &- a_{t(i,2j-2,2k-2)}^f + a_{t(i,2j-1,2k-2)}^f \end{aligned} \quad (35)$$

$$\begin{aligned}
 Sc_{i,j,k}^c &= r_{i,2j-2,2k-2}^f + r_{i,2j-2,2k-1}^f \\
 &+ r_{i,2j-1,2k-2}^f + r_{i,2j-1,2k-1}^f
 \end{aligned}
 \tag{36}$$

the residuals on the fine grid level  $r_{i,j,k}^f$  are calculated from the current iterative values of  $\hat{\phi}_{i,j,k}^f$  using the following relation:

$$\begin{aligned}
 r_{i,j,k}^f &= -a_{p(i,j,k)}^f \hat{\phi}_{i,j,k}^f + a_{e(i,j,k)}^f \hat{\phi}_{i+1,j,k}^f \\
 &+ a_{n(i,j,k)}^f \hat{\phi}_{i,j+1,k}^f + a_{t(i,j,k)}^f \hat{\phi}_{i,j,k+1}^f \\
 &+ a_{w(i,j,k)}^f \hat{\phi}_{i-1,j,k}^f + a_{s(i,j,k)}^f \hat{\phi}_{i,j-1,k}^f \\
 &+ a_{b(i,j,k)}^f \hat{\phi}_{i,j,k-1}^f + Sc_{i,j,k}^c
 \end{aligned}
 \tag{37}$$

A typical two-level multigrid iterative algorithm consists of restriction, relaxation on the coarse grid and prolongation. After a number of relaxation sweeps, such as TDMA sweeps, on the fine grid level, the residuals are calculated using Equation (37) and are restricted to the coarse grid using Equations (29-36). The restricted residuals are then used as the source terms in Equation (28) and relaxation sweeps are used to solve Equation (28) on the coarse level. The solutions to Equation (28) are then utilized as the corrections to be prolonged back to the fine grid using the following relations to update the current iterative solution of  $\hat{\phi}_{i,j,k}^f$ ,

$$\begin{aligned}
 \hat{\phi}_{i,2j-2,2k-2}^f &= \hat{\phi}_{i,2j-2,2k-2}^f + \phi_{i,j,k}^c \\
 \hat{\phi}_{i,2j-2,2k-1}^f &= \hat{\phi}_{i,2j-2,2k-1}^f + \phi_{i,j,k}^c \\
 \hat{\phi}_{i,2j-1,2k-2}^f &= \hat{\phi}_{i,2j-1,2k-2}^f + \phi_{i,j,k}^c \\
 \hat{\phi}_{i,2j-1,2k-1}^f &= \hat{\phi}_{i,2j-1,2k-1}^f + \phi_{i,j,k}^c
 \end{aligned}
 \tag{38}$$

Equation (38) provides the prolongation formulation in the AC multigrid calculation. Obviously, the restriction (Equations (29-36)) and prolongation (Equation (38)) are second-order accuracy in space and no extra interpolations are needed. The AC-MG solution procedure contains two parts. The first part consists of a subroutine of TDMA sweeps, which is controlled by the residual convergence rate. A flowchart of the TDMA solver is depicted in Figure 5. If the total residual before iteration  $n$  on the current mesh is  $R^n = \sum_{i,j,k} r_{i,j,k}^n$  and the residual after iteration  $n$  is  $R^{n+1}$ , then another TDMA sweeping iteration is performed if the residual convergence rate satisfies  $R^{n+1} \geq f \cdot R^n$  where the value for  $f$  is usually set to 0.5 [23]. If the convergence rate is lower than 0.5, i.e.  $R^{n+1}/R^n > f$ , a correction on the coarser grid is required, which invokes the second part of the AC-MG solution procedure. A schematic figure of the three-level AC-MG solution procedure will be shown in Figure 6.

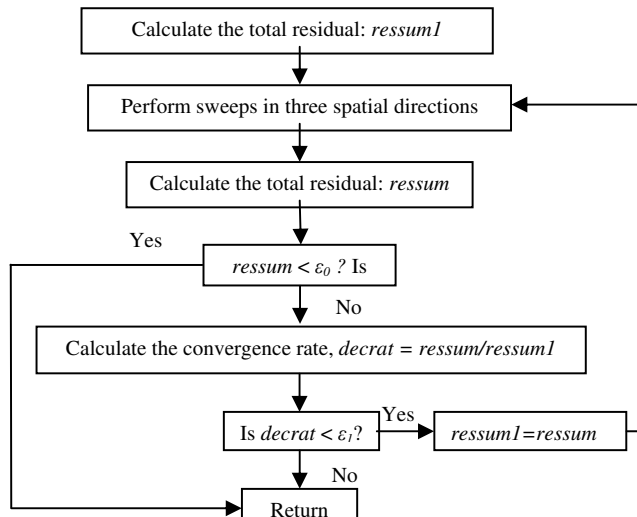


Fig. 5. Flowchart of the TDMA solver controlled by the residual convergence rate.

In order to check the sensitivity of the numerical results to mesh size, three different grid systems were tested. They consisted of  $18 \times 42 \times 16$ ,  $30 \times 82 \times 30$  and  $50 \times 162 \times 58$  nodes in the  $x$ ,  $y$ , and  $z$  directions, respectively. The results from the last two grid systems were very close to each other and local temperature differences were less than 0.1%. Since less computational time and computer memory were needed for the second grid system, it was employed in the final simulation.

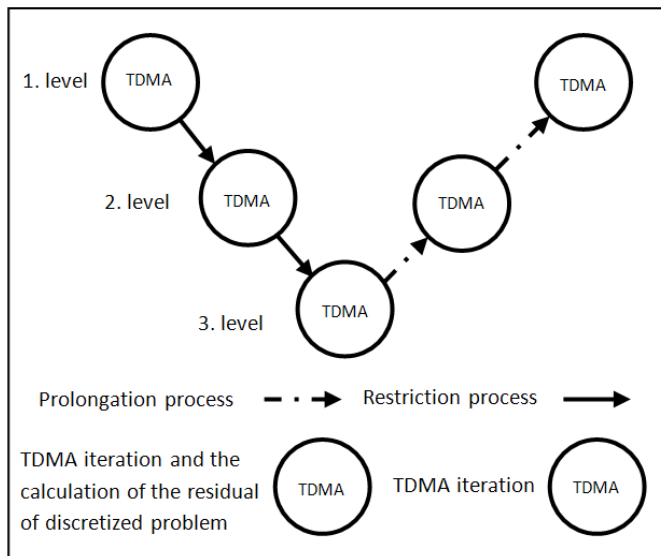


Fig. 6. A schematic of the three-level AC-MG solution procedure.

The total grid number is 73,800 ( $N_x \times N_y \times N_z$  is  $30 \times 82 \times 30$ ) for the domain. This type of a fine grid mesh for the  $y$  and  $z$  directions was chosen in order to properly resolve the velocity and viscous shear layers, and to more accurately define the conjugate heat transfer at the surface of the channel, thereby improving the temperature resolution. Furthermore, comparison with standard theoretical or numerical results indicates that the finer the mesh size the higher the numerical accuracy. The reasons for the comparative coarse discretization for the  $x$ -direction are: (i) with the exception of the inlet region, the temperature gradients are small compared to the gradients occurring in other directions; and (ii) The CPU time as well as the memory storage required increases dramatically as the number of grid nodes is increased.

### 3. Validation of the code

#### 3.1 Velocity field

The velocity field can be determined analytically using a more direct approach. As illustrated in Figure 7, the following relations represent the reasonable results for this type of problem by Shah and London [24],

$$u = -\frac{16c_1 a^2}{\pi^3} \sum_{n=1,3,\dots}^{\infty} \frac{1}{n^3} (-1)^{(n-1)/2} \times \left[ 1 - \frac{\cosh(n\pi y / 2a)}{\cosh(n\pi b / 2a)} \right] \cos\left(\frac{n\pi z}{2a}\right) \tag{39}$$

$$u_m = -\frac{c_1 a^2}{3} \left[ 1 - \frac{192}{\pi^5} \left(\frac{a}{b}\right) \sum_{n=1,3,\dots}^{\infty} \frac{1}{n^5} \tanh\left(\frac{n\pi b}{2a}\right) \right] \tag{40}$$

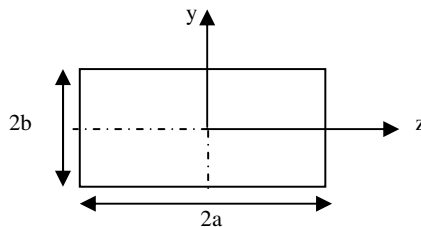


Fig. 7. A schematic of the rectangular channel.

This velocity profile is in excellent agreement with the experimental results. Since Equation (39) involves considerable computational complexity, a simple approximation in the following form for the aspect ratio  $\alpha^* \leq 0.5$  is proposed [24],

$$\frac{u}{u_{\max}} = \left[ 1 - \left(\frac{y}{b}\right)^n \right] \left[ 1 - \left(\frac{z}{a}\right)^m \right] \tag{41}$$

where  $m$  and  $n$  are derived from below relations,

$$m = 1.7 + 0.5(\alpha^*)^{-1.4} \quad (42)$$

$$n = \begin{cases} 2 & \text{for } \alpha^* \leq 1/3 \\ 2 + 0.3(\alpha^* - 1/3) & \text{for } \alpha^* \geq 1/3 \end{cases} \quad (43)$$

The integration of Equation (41) over the duct cross section yields,

$$\frac{u}{u_m} = \left(\frac{m+1}{m}\right)\left(\frac{n+1}{n}\right) \left[1 - \left(\frac{y}{b}\right)^n\right] \left[1 - \left(\frac{z}{a}\right)^m\right] \quad (44)$$

$$\frac{u_{\max}}{u_m} = \left(\frac{m+1}{m}\right)\left(\frac{n+1}{n}\right) \quad (45)$$

With  $fRe$  of Equation (46),  $u_m$  for the rectangular ducts can be expressed in a closed form as,

$$fRe_{D_h} = 24(1 - 1.3553\alpha^* + 1.9467\alpha^{*2} - 1.7012\alpha^{*3} + 0.9564\alpha^{*4} - 0.2537\alpha^{*5}) \quad (46)$$

$$u_m = -\frac{8c_1a^2}{fRe_{D_h} \left[1 + (a/b)^2\right]} \quad (47)$$

where

$$c_1 = \frac{dp/dx}{\mu} = \frac{\Delta p/L_x}{\mu} \quad (48)$$

Substituting Equations (46) and (48) into Equation (47), the mean velocity for a given pressure drop,  $u_m$  can be obtained. Then, using the resulting value for  $u_m$  and Equations (42-44), the approximate analytical velocity distribution in the microchannel as shown in Figure 8 can be obtained. The numerically determined velocity profile developed here is illustrated in Figure 9. Comparison of the analytical and numerical results indicates that while the numerical code exactly represents the general trend of the results, there is some disparity between the analytical and numerical results. The small difference of the velocity profile between Figures 8 and 9 is due to the approximations in the analytical solution described in Equations (41) and (44). But clearly, as evidenced by the magnitude of the mean velocities and the Reynolds numbers obtained from the different methods, the agreement between the two methods is quite good and provides sufficient evidence for validation of the numerical method. In this comparison, the thermophysical properties of water were chosen at a temperature of 293 K (20°C). Because the thermophysical properties are temperature dependent, especially the liquid viscosity, the velocity and the Reynolds numbers are different under the same pressure drop conditions. This issue will be discussed in more detail later.

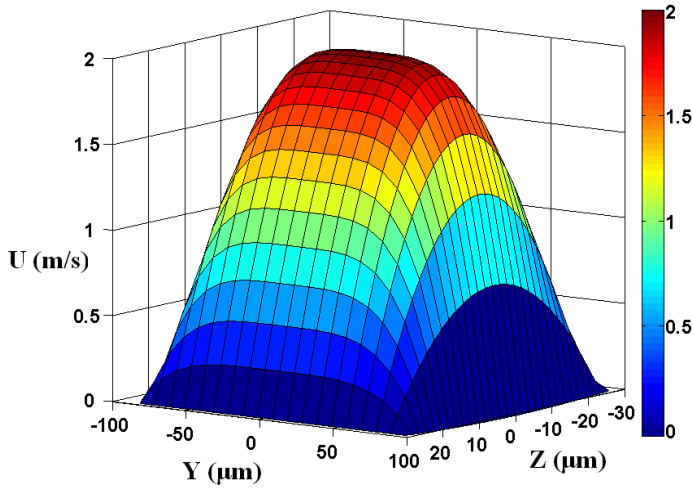


Fig. 8. Velocity field in channel from the approximate analytical expression Equation (44),  $\Delta p=50 \text{ kPa}$ ,  $Re=92.68$ ,  $T_{reference}=20^\circ\text{C}$ ,  $u_m=1.0779 \text{ m/s}$ .

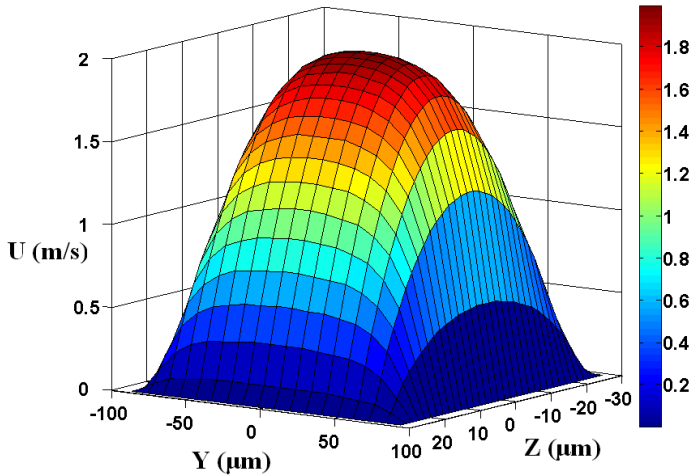


Fig. 9. Velocity field in channel from the numerical calculation,  $\Delta p = 50 \text{ kPa}$ ,  $Re=92.383$ ,  $T_{reference}=20^\circ\text{C}$ ,  $u_m=1.1032\text{m/s}$ ,  $u_{max}=1.997 \text{ m/s}$ .

Figure 10 compares the analytical friction coefficient as determined from Equation (46) with the numerical results obtained using the following procedure, should be noted that,  $f_{Darcy}=4f$ . The mass flow rate is calculated from the velocity as,

$$\dot{m} = \sum \sum \rho_f .u(i = \text{constant}, j, k) \Delta y \Delta z \tag{49}$$

and then, the mean velocity is obtained as

$$u_m = \frac{\dot{m}}{\rho_f A} = \frac{\dot{m}}{\rho_f HW} \tag{50}$$

then using Equation (51), the friction factor can be determined as Equation (52),

$$\Delta p = f \frac{4L_x}{D_h} \frac{\rho_f u_m^2}{2} \tag{51}$$

$$f_{Darcy} Re_{D_h} = 2 \frac{\Delta p D_h^2}{u_m L_x \mu_f} \tag{52}$$

In References [25-27], the friction coefficient,  $f_{Darcy} Re$ , is determined numerically for different duct cross-sections. For the rectangular channel with an aspect ratio (height to width) of 3-1 ( $H:W$ ), which approximates the geometry used here,  $180\mu m \times 57\mu m$ , the Darcy friction factor-Reynolds number product,  $f_{Darcy} Re$ , is 69. The agreement between the numerical calculations here and the calculations obtained by others [25-27] represents that the numerical code developed here is quite accurate for the fully developed laminar flow.

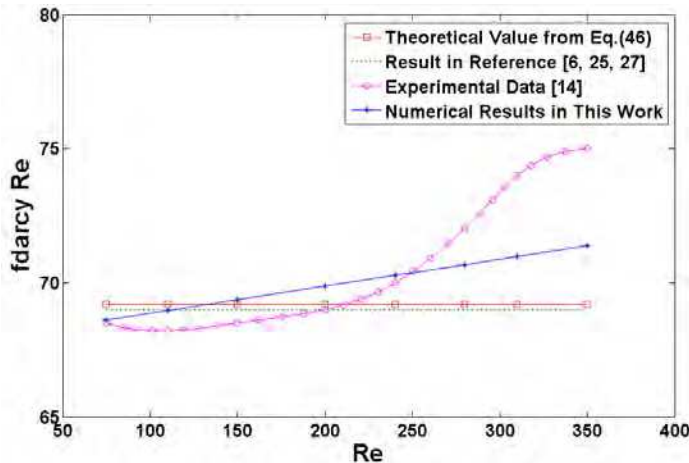


Fig. 10. Comparison among the numerical calculations, the analytical and the experimental data for the friction coefficient.

The length required for the formation of a fully developed laminar profile in a microchannel can be estimated by the following analytical relation [26] that is developed for a round tube,

$$\frac{L_e}{D_h} = 0.0575 Re_{D_h} \tag{53}$$

For a hydraulic diameter of  $D_h = 86.58 \mu m$  and for  $Re = 160$  the entrance length is  $796.5 \mu m$ . In References [25-27], it is noted that the shape of the entrance is very important, with much

shorter entrance lengths occurring for square-edged entrances than for rounded ones. Thus, because the flow entrance length may be less than 5% of the total length for a rectangular channel heat sink, the assumption of fully developed laminar flow over the entire length of the microchannel is acceptable for the heat transfer analysis, particularly in cases such as this where the Reynolds number is less than 200 (or low mass flow rates).

### 3.2 Heat transfer

The code was first validated for one dimensional heat conduction by comparing the results with a 1D analytical solution of heat conduction with a specified boundary condition [25]. The agreement was quite good and indicated very good correlation between the numerical results and the 1D analytical solution, Secondly, using conservation of energy, it can be shown that the maximum possible temperature rise between the fluid inlet and outlet can be expressed as:

$$\Delta T_{f,con} = \frac{q_s \cdot A_s}{\dot{m} \cdot c_p} \tag{54}$$

In addition, the average temperature rise between the inlet and outlet of the channel can be determined from the numerical analysis as follow,

$$\begin{aligned} \Delta T_{f,ave} &= \bar{T}_f(x=L_x) - \bar{T}_f(x=0) \\ &= \frac{\left\{ \sum \sum \rho_f \cdot u \cdot c_p \cdot T \cdot \Delta y \Delta z \right\}_{i=outlet, j, k}}{\dot{m} \cdot c_p} \\ &\quad - \frac{\left\{ \sum \sum \rho_f \cdot u \cdot c_p \cdot T \cdot \Delta y \Delta z \right\}_{i=inlet, j, k}}{\dot{m} \cdot c_p} \end{aligned} \tag{55}$$

In this work, three different cases ( $q_s=90 \text{ W/cm}^2$ ,  $\Delta p=50, 15$  and  $6 \text{ kPa}$ ) were investigated. Comparison of the results in Table 2, indicates that the difference between  $\Delta T_{f,ave}$  and  $\Delta T_{f,con}$  is small. This issue also is illustrated in Figure 11. Differences of this magnitude can be attributed to (i) Equation (54) is the maximum possible temperature rise in the bulk liquid from the energy balance; (ii) the mesh size is not as fine as required (infinitesimal), hence the accuracy of the statistical result from Equation (55) is limited.

$\Delta p(\text{kPa})$	50	15	6
$Re$	162.68	85.60	47.32
$\Delta T_{f,con} (\text{°C})$	14.62	36.82	78.57
$\Delta T_{f,ave} (\text{°C})$	12.79	35.10	77.16

Table 2. Comparison between  $\Delta T_{f,ave}$  and  $\Delta T_{f,con}$  for  $\Delta p=50, 15$  and  $6 \text{ kPa}$ ,  $q_w=90 \text{ W/cm}^2$ .

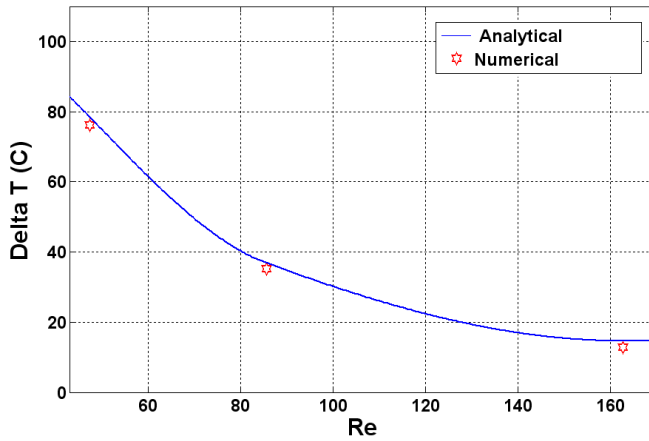


Fig. 11. Comparison between the numerical and analytical results for temperature differences upon the Reynolds number.

### 4. Results and discussion

The following four subsections are devoted to the local temperature distributions, the average and bulk characteristics, the local heat flux distributions and the Convergence Performance for the Pressure Correction Equations in microchannel heat sinks.

#### 4.1 Local temperature distributions

Figure 12 shows a velocity field in a microchannel at  $\Delta p=50\text{ kPa}$ . As discussed previously, the thermophysical properties of the water are based upon the estimated liquid bulk temperature. As can be seen by comparison with the results shown in Figure 9, for the same pressure drop along the channel, the thermal properties, velocity profile, mean velocity and Reynolds number are all mainly different.

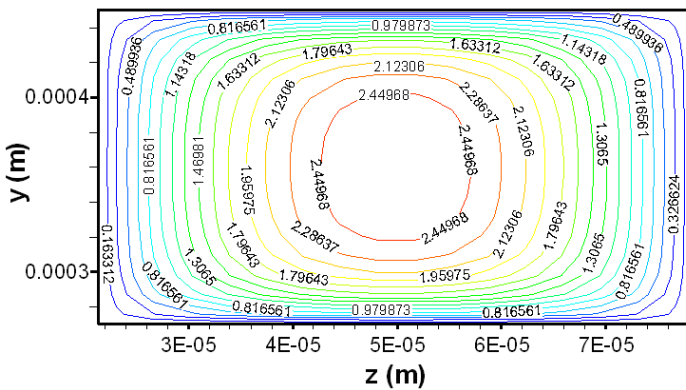


Fig. 12. X- component velocity field from the numerical calculation,  $\Delta p=50\text{ kPa}$ ,  $Re=162.68$ ,  $T_{reference}=32^\circ\text{C}$ ,  $u_m=1.44\text{ m/s}$ ,  $u_{max}=2.61\text{ m/s}$ .

As shown, a variation in the reference temperature,  $T_{reference}$  from 20 to 32°C, changes the mean velocity from 1.1032 to 1.44 m/s, and results in a corresponding change in the Reynolds number from 95.38 to 162.68. The numerical results for the temperature distribution in the heat sinks are shown in Figures 13, 14, 15, 16 and 17 for different locations along the channel. Figures 13, 14 and 15 show the local cross-sectional temperature distribution in the  $y$ - $z$  plane at  $x=0$ ,  $x=L_x/2$  and  $x=L_x$ , respectively. As shown in Figure 13, the temperature of the liquid at the inlet is initially uniform (at 20°C). The temperature profiles shown in Figures 14 and 15 are identical in shape due to the assumption of hydrodynamic fully developed flow, but the magnitudes of the temperature are different.

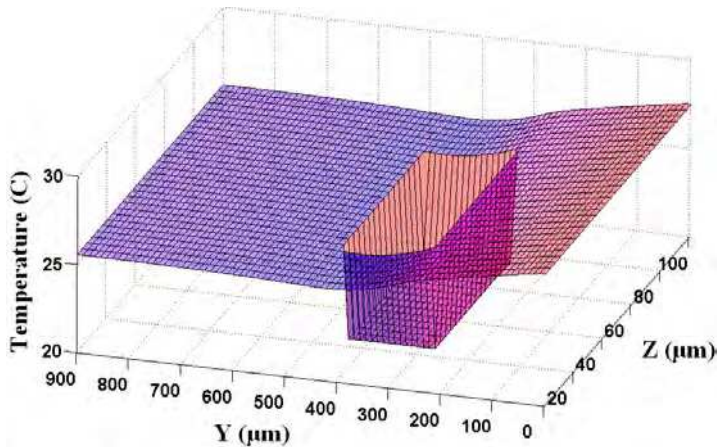


Fig. 13. Local temperature distribution in  $y$ - $z$  plane at  $x=0$ , ( $\Delta p=50$  kPa,  $Re=162.68$ ,  $T_{reference}=32^\circ\text{C}$ ,  $u_m=1.44$  m/s).

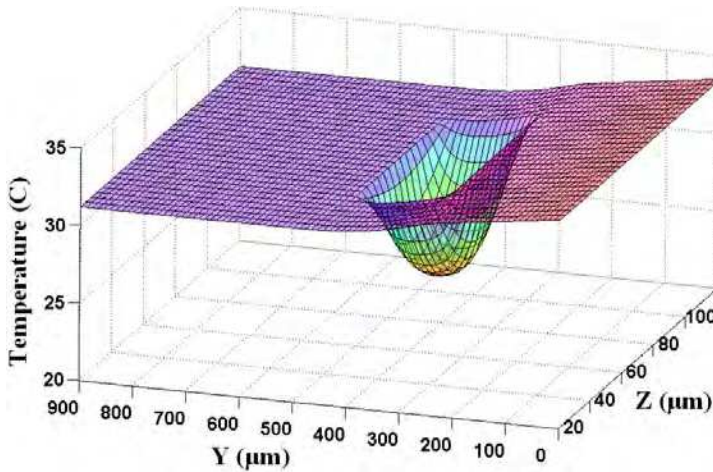


Fig. 14. Local temperature distribution in  $y$ - $z$  plane at  $x=L_x/2$ , ( $\Delta p=50$  kPa,  $Re=162.68$ ,  $T_{reference}=32^\circ\text{C}$ ,  $u_m=1.44$  m/s).

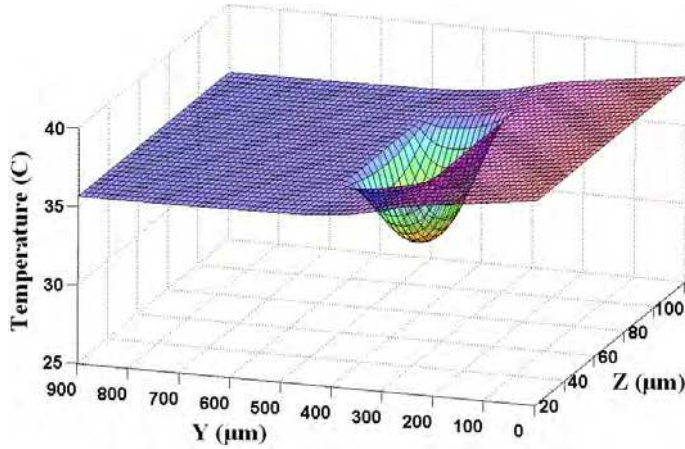


Fig. 15. Local temperature distribution in  $y$ - $z$  plane at  $x = L_x$ , ( $\Delta p = 50 \text{ kPa}$ ,  $Re = 162.68$ ,  $T_{reference} = 32^\circ\text{C}$ ,  $u_m = 1.44 \text{ m/s}$ ).

Figure 16 shows the temperature contours in the heat sink at the outlet of the channel and Figure 17 shows the local temperatures inside the channel. It is noted in Figure 17 that the temperature is highest at the channel corner. This is due to the low velocity of the flow and the resulting high concentration of heat flux. From these calculations it is apparent that there is a 2–3°C temperature difference between the bottom wall of the substrate and the bottom surface of the channel.

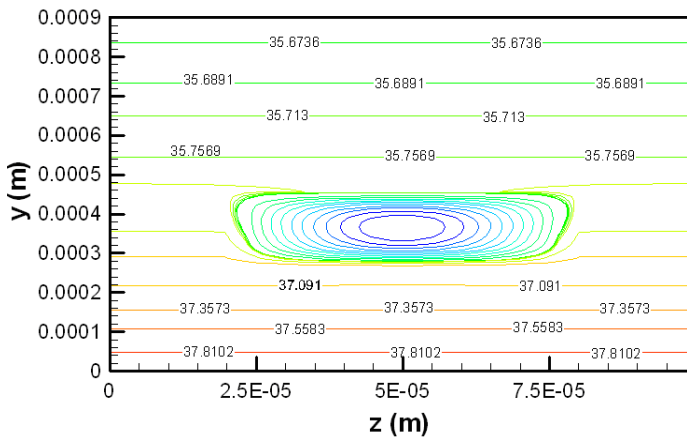


Fig. 16. Contour of temperature in the heat sink at the cross-section of the outlet of the channel ( $\Delta p = 50 \text{ kPa}$ ,  $Re = 162.68$ ,  $T_{reference} = 32^\circ\text{C}$ ,  $u_m = 1.44 \text{ m/s}$ ).

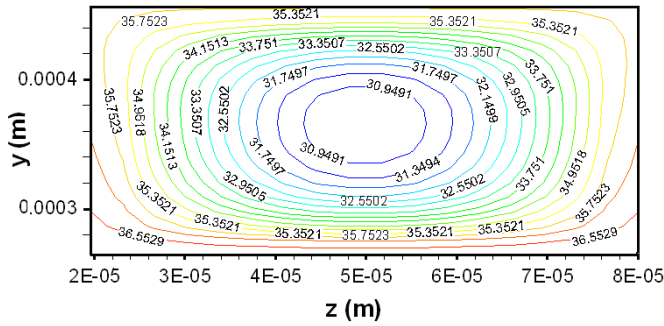


Fig. 17. Contour of local temperature inside the channel at the cross-section of the outlet of the channel ( $\Delta p=50$  kPa,  $Re=162.68$ ,  $T_{reference}=32^{\circ}C$ ,  $u_m=1.44$  m/s).

The temperature distribution can be showed obviously in Figures 18, 19 and 20, which indicate the local temperature distribution in the  $x$ - $y$  plane at  $z=L_z/2$  for the three cases with  $q_s=90$  W/cm<sup>2</sup>, at  $\Delta p=50, 15$  and  $6$  kPa, respectively.

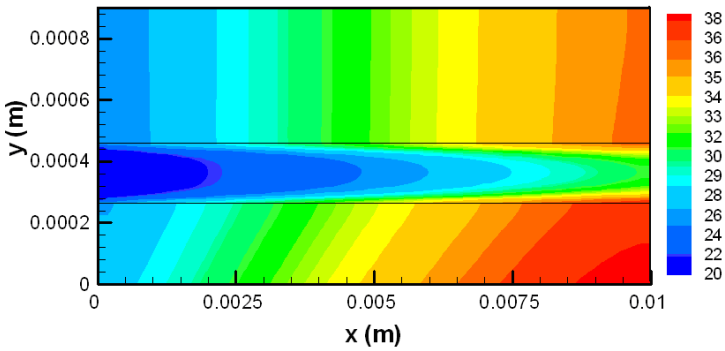


Fig. 18. Local temperature distribution in  $x$ - $y$  plane at  $z=L_z/2$  ( $\Delta p=50$  kPa,  $Re=162.68$ ,  $T_{reference}=32^{\circ}C$ ,  $u_m=1.44$  m/s).

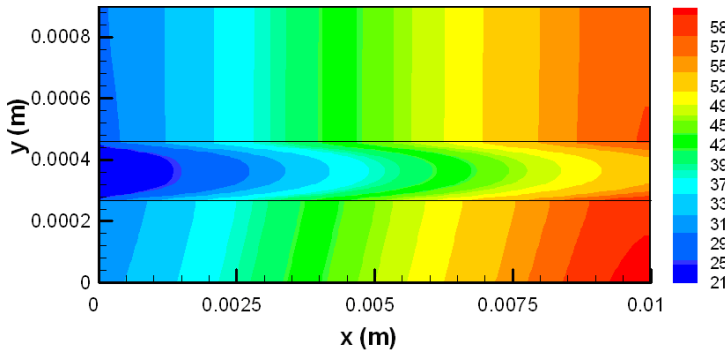


Fig. 19. Local temperature distribution in  $x$ - $y$  plane at  $z=L_z/2$  ( $\Delta p=15$  kPa,  $Re=85.60$ ,  $T_{reference}=48^{\circ}C$ ,  $u_m=0.57$  m/s).

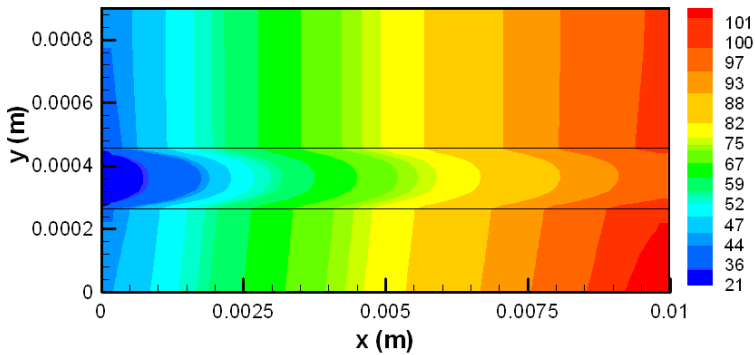


Fig. 20. Local temperature distribution in  $x$ - $y$  plane at  $z=L_z/2$  ( $\Delta p=6$  kPa,  $Re=47.32$ ,  $T_{\text{reference}}=57^\circ\text{C}$ ,  $u_m=0.271$  m/s).

The water flow is clearly specified in these Figures, which when combined with Figures 13, 14, 15, yield detailed information about the temperature distribution in the micro-heat sink. The temperature at the outlet for the case of  $\Delta p=6$  kPa is higher than  $100^\circ\text{C}$  where boiling may occur. Therefore, the numerical solution for single-phase flow may not be valid there. The temperature increases along the longitudinal  $x$ -direction over the channel inner walls. There are very slight changes in the temperature gradient in the  $x$ -direction at the channel bottom wall, Figure 21, and the channel top wall, Figure 22.

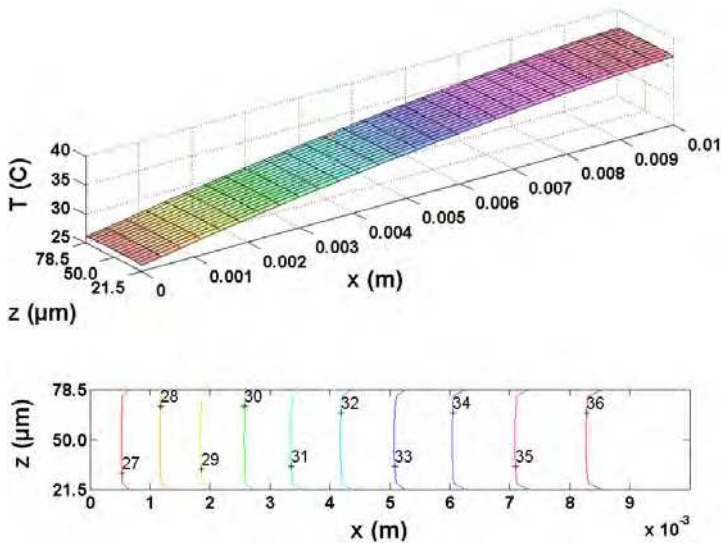


Fig. 21. Numerical predictions of local temperature distribution in the unit cell bottom wall.

In fact, a linear temperature rise can be regarded as a good approximation for both planes. The temperature along the transverse  $z$ -direction is virtually constant for all the  $x$ - $z$  planes just discussed.

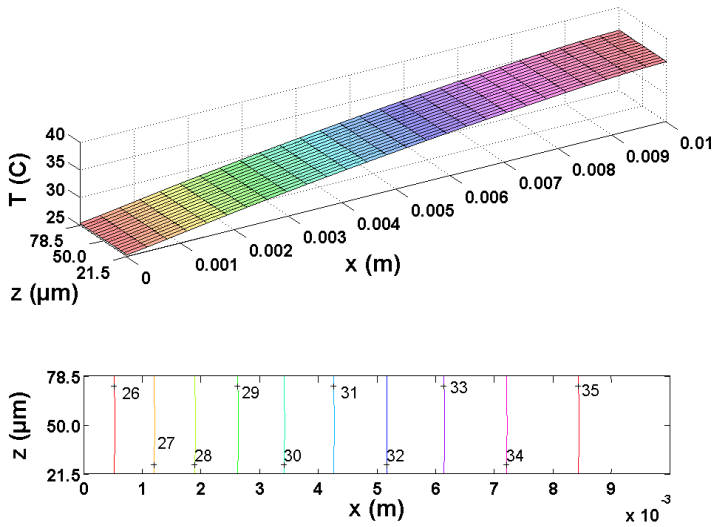


Fig. 22. Numerical predictions of local temperature distribution in the unit cell top wall.

The temperatures of the side walls vary noticeably in the transverse  $y$ -direction. As expected, the temperature decreases from the unit cell bottom wall to the unit cell top wall. Figure 23 shows higher temperatures for small  $y$  values close to the channel bottom wall.

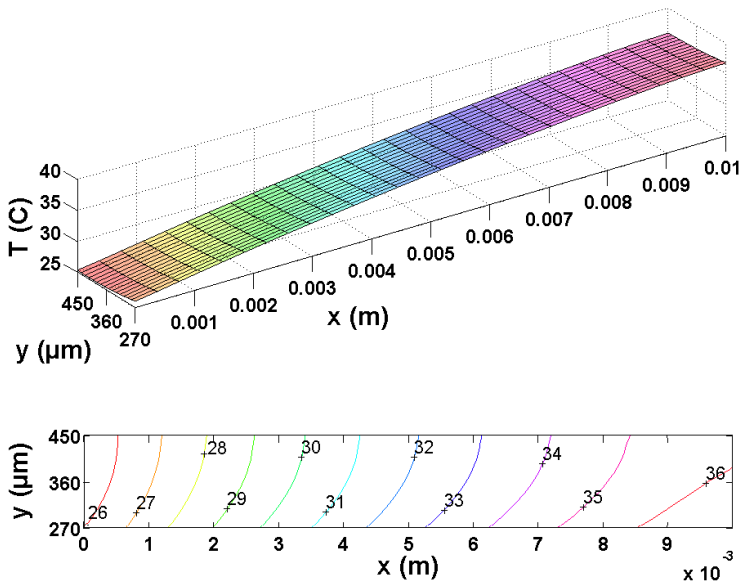


Fig. 23. Numerical predictions of local temperature distribution in the unit cell side walls.

## 4.2 Average and bulk characteristics

In order to evaluate the local (averaged on the channel circumference) heat transfer characteristics along the flow direction, the convective heat transfer coefficient and Nusselt number, must be defined. The longitudinal convective heat transfer coefficient is defined as

$$\bar{h}_x = \frac{\bar{q}_{s,\Gamma}(x)}{\Delta\bar{T}(x)} \quad (56)$$

and the averaged longitudinal Nusselt number as

$$\overline{Nu}_x = \frac{\bar{h}_x \cdot D_h}{k_f} \quad (57)$$

The averaged longitudinal local heat flux along the perimeter of the inner wall of the channel in Equation (56) is defined as,

$$\begin{aligned} \bar{q}_{s,\Gamma}(x) &= -k_s \left( \frac{\partial T_s(x,y,z)}{\partial n} \right) \Big|_{\Gamma} \\ &= -k_f \left( \frac{\partial T_f(x,y,z)}{\partial n} \right) \Big|_{\Gamma} \end{aligned} \quad (58)$$

and the longitudinal mean temperature difference in Equation (56) is defined as,

$$\Delta\bar{T}(x) = \bar{T}_{s,\Gamma}(x) - \bar{T}_f(x) \quad (59)$$

$$\bar{T}_{s,\Gamma}(x) = \frac{\sum_{\Gamma} T_{s,\Gamma}(i,j,k)}{N_{\Gamma}} \quad (60)$$

$$\bar{T}_f(x) = \frac{\left\{ \sum \sum \rho_f \cdot u \cdot c_p \cdot T \cdot \Delta y \Delta z \right\}_{i=\text{constant},j,k}}{\dot{m} \cdot c_p} \quad (61)$$

where  $N_{\Gamma}$  is the total number of nodes along the perimeter of the inner wall (here  $N_{\Gamma} = 2 \times 16 + 2 \times 16$ ). The averaged longitudinal inner wall temperature  $\bar{T}_{s,\Gamma}$  and the averaged local heat flux  $\bar{q}_{s,\Gamma}$  are mathematically averaged along the perimeter of the inner wall, and the longitudinal bulk liquid temperature  $\bar{T}_f$  is averaged according to energy conservation. With Equations (56)-(59), the longitudinal heat transfer coefficient variation and the longitudinal Nusselt number variation for these three cases can be determined and are shown in Figures 24 and 25, respectively.

From these two Figures it can be concluded that the variations of the heat transfer coefficient and the Nusselt number along the flow direction is quite small for this type of microchannel heat sink after the thermal entrance lengths. Comparisons between the average Nusselt number for the different heat flux and same Reynolds number are shown in Figure 26.

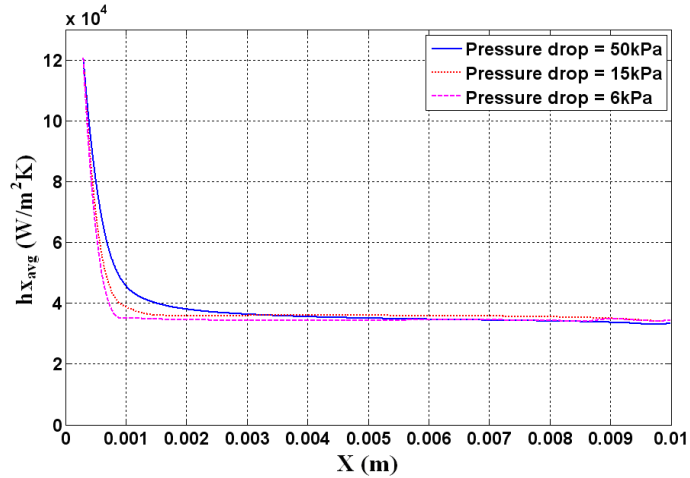


Fig. 24. Distribution of heat transfer coefficient along the channel at specified pressure drop.

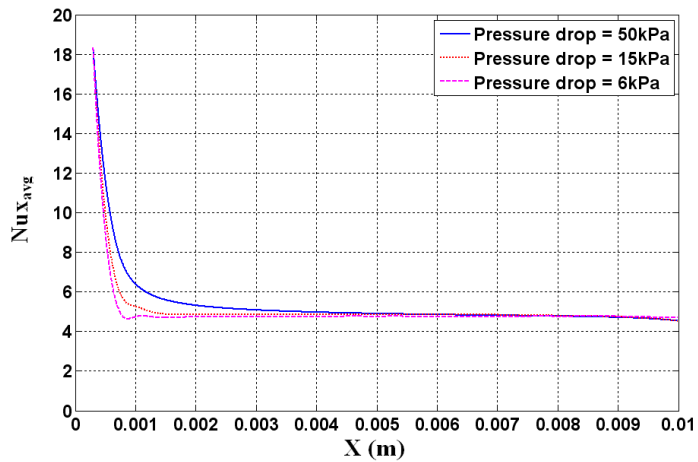


Fig. 25. Nusselt number variation along the channel at specified pressure drop.

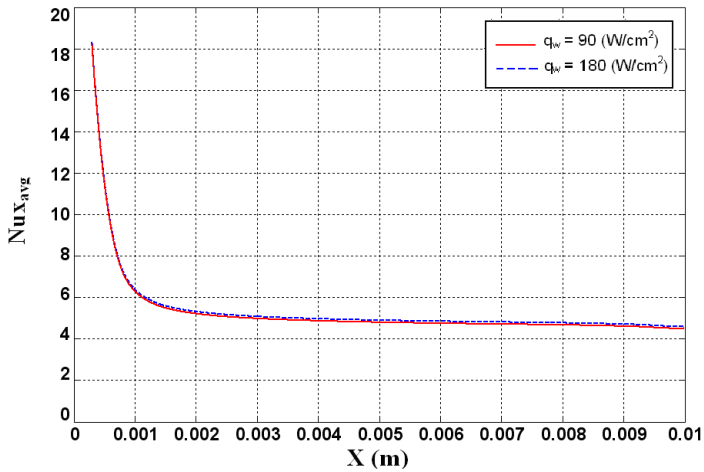


Fig. 26. Comparisons between the average Nusselt numbers.

These two trends are identical; this is because the Nusselt number for laminar flow is determined solely by the channel geometry and the local flow conditions.

Figure 27 shows the fluid bulk temperature and the average temperatures of the top, bottom and side channel walls, as the functions of the longitudinal distance  $x$ , for  $\Delta p = 50 \text{ kPa}$ . The fluid bulk temperature increases quasi-linearly along the  $x$ -direction, and it almost reaches the wall temperature at the exit of the microchannel. Overall, the average temperatures of side walls are slightly larger than top wall and smaller than bottom wall, because the convective resistance is much smaller for the close space between the side walls. While, in Figure 28 that is  $\Delta p = 6 \text{ kPa}$ , due to low liquid velocity and low convective heat transfer, temperature difference will be increased between the solid and liquid, especially in the inlet region of the channel.

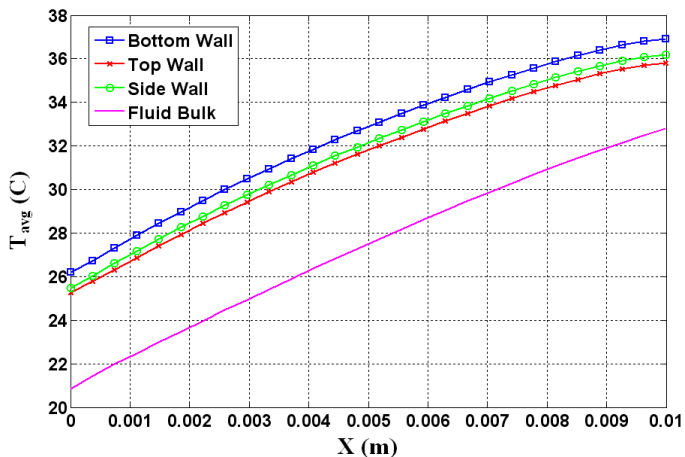


Fig. 27. Mean temperature variations along the channel at the top, bottom and side walls and in bulk liquid for  $\Delta p = 50 \text{ kPa}$ .

Large temperature gradients near the inlet region are mainly to induce significant thermal stresses and, therefore, must be carefully considered in the practical sink design in order to avoid the mechanical failure. The quasi-linear trend is not validated for the low Reynolds numbers as be shown in Figure 28. In Figure 28 a large portion of heat is conducted into the front part of the heat sink due to the low liquid velocity, and so the temperature gradient between the top and bottom walls is much small and approaching to the zero value.

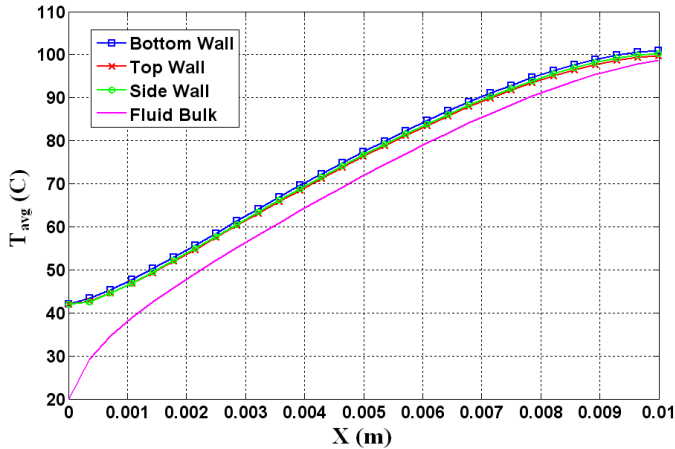


Fig. 28. Mean temperature variations along the channel at the top, bottom and side walls and in bulk liquid for  $\Delta p = 6 \text{ kPa}$ .

As the flow develops and the boundary layers grow in the longitudinal direction, the average heat transfer coefficients (Figure 29) gradually decrease in magnitude. The heat transfer coefficients are expected and, indeed, are larger at the side walls than at the top and bottom walls.

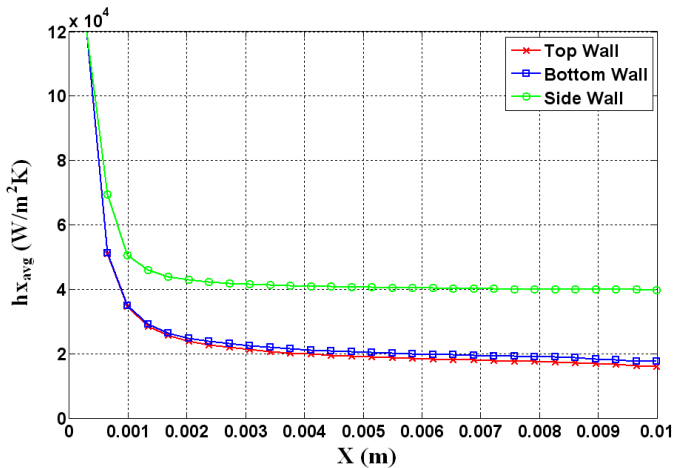


Fig. 29. Average heat transfer coefficient distributions along the channel.

### 4.3 Local heat flux distribution

Figs 30, 31 and 32 illustrate the heat flux distribution along the channel walls for  $\Delta p=50\text{ kPa}$ ,  $Re=162.68$ ,  $T_{reference}=32^\circ\text{C}$ ,  $u_m=1.44\text{ m/s}$ . For all the channel walls, higher heat fluxes are encountered near the channel inlet. This is attributed to the thin thermal boundary layer in the developing region. The heat fluxes vary around the channel periphery, approaching zero in the corners where the flow is weak for a rectangular channel. Figure 32 shows the heat flux along the channel side walls is higher than along the channel top and bottom walls (almost two orders of magnitude larger than those at the top and bottom walls) due to the short distance between the channel side walls and the large velocity gradient present. The local heat fluxes at both the bottom and top walls (Figures 30 and 31, respectively) show significant variation in the transverse  $z$ -direction, unlike the fluxes at the side walls (Figure 32), which are nearly uniform everywhere but in the inlet and corner regions.

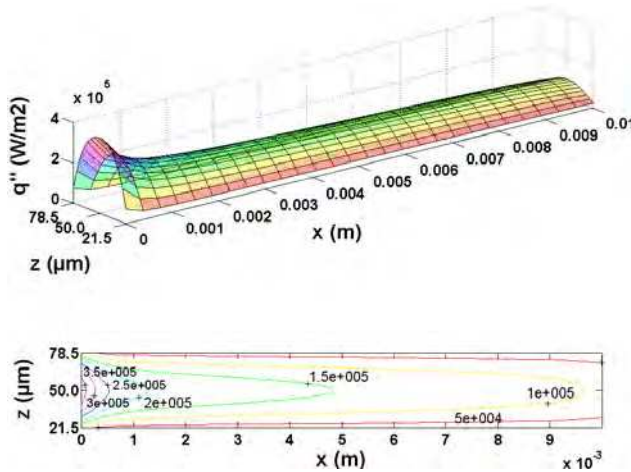


Fig. 30. Numerical predictions of local heat flux distribution for the channel bottom wall.

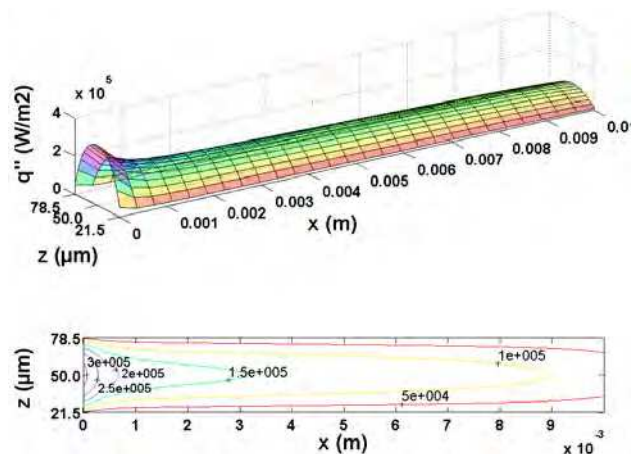


Fig. 31. Numerical predictions of local heat flux distribution for the channel top wall.

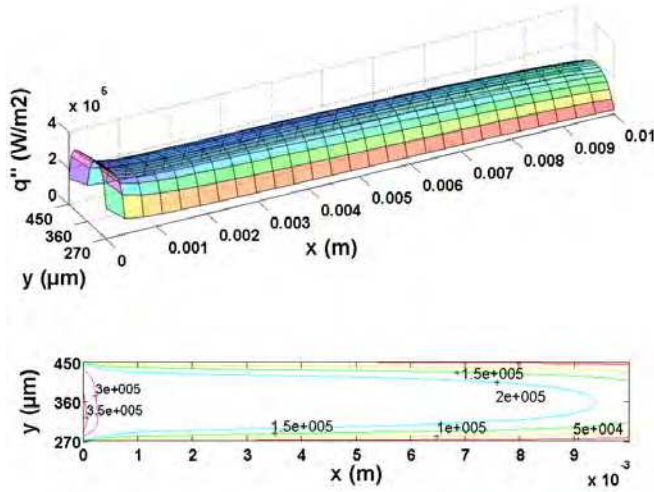


Fig. 32. Numerical predictions of local heat flux distribution for the channel side walls.

**4.4 Convergence performance for the pressure correction equations**

For the microchannel heat sink model, illustrated in Figure 1, the total number of control volumes in the heat sink and inside the channel were set to  $N_x \times N_y \times N_z = 30 \times 82 \times 30$  and  $N_x \times N_y \times N_z = 30 \times 16 \times 16$  in the three spatial directions, respectively. The multigrid scheme, as discussed in the previous section, was implemented in the two cross-streamwise directions, which consisted of four grid levels from the finest grid ( $30 \times 16 \times 16$ ) to the coarsest grid ( $30 \times 2 \times 2$ ). The multigrid behavior followed the typical V-cycle pattern. The entire residual convergence history with the AC-MG algorithm is depicted in Figure 33.

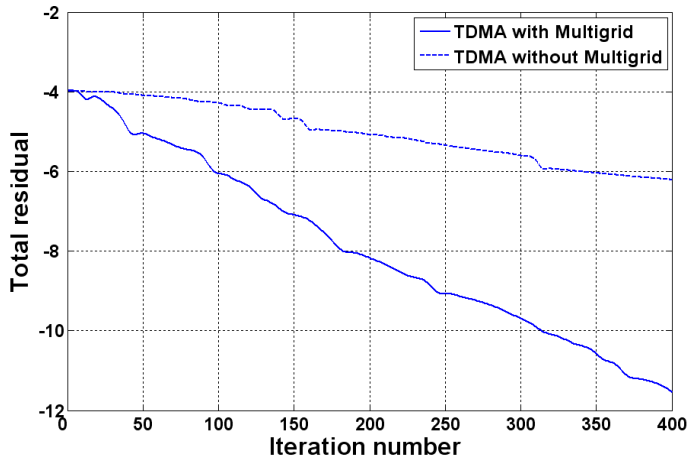


Fig. 33. Residual convergence history of the pressure Poisson equation.

The results are compared with the solution procedure that used only the TDMA solver without a multigrid correction. The TDMA solver with the AC-MG algorithm was capable of efficiently driving the residual down to the level of the computer machine round-off error within 400 AC-MG cycles. The residual was driven down by about twelve orders of magnitude.

## 5. Conclusion

A three-dimensional mathematical model, developed using incompressible laminar Navier-Stokes equations of motion, is capable of predicting correctly the flow and conjugate heat transfer in the microchannel heat sink. The microchannel heat sink model consists of a 10 mm long silicon substrate, with rectangular microchannels, 57  $\mu\text{m}$  wide and 180  $\mu\text{m}$  deep, fabricated along the entire length. A finite volume numerical code with a multigrid technique, based on additive correction multigrid (AC-MG) scheme, that is a high-performance solver, was developed to solve the steady incompressible laminar Navier-Stokes (N-S) equations, over a collocated Cartesian grid arrangement. Higher Reynolds numbers are beneficial at reducing both the water outlet temperature and the temperatures within the heat sink, also at the expense of greater pressure drop. By the magnitude of the mean velocities and the Reynolds numbers obtained from the analytical and numerical methods, the agreement between the two methods is quite good and provides sufficient evidence for validation of the numerical method. The variations of the heat transfer coefficient and the Nusselt number along the flow direction is quite small for this type of microchannel heat sink after the thermal entrance lengths. The heat flux along the channel side walls is higher than along the channel top and bottom walls (almost two orders of magnitude larger than those at the top and bottom walls) due to the short distance between the channel side walls and the large velocity gradient present. The temperature is highest at the channel corner; this is due to the low velocity of the flow and the resulting high concentration of heat flux. The results indicate that the thermophysical properties of the liquid can significantly influence both the flow and heat transfer in the microchannel heat sink. The bulk liquid temperature is shown to vary in a quasi-linear form along the flow direction for high fluid flow rates, but not for low flow rates (low Reynolds number).

## 6. References

- [1] D.B. Tuckerman, R.F. Pease, "High-Performance Heat Sinking for VLSI, " *IEEE Electronic Devices Letters EDL-2* (1981) 126-129.
- [2] S.P. Jang, S. Kim, K.W. Paik, 2003, "Experimental Investigation of Thermal Characteristics for a Microchannel Heat Sink Subject to an Impinging Jet, Using a Micro Thermal Sensor Array," *Sens. Actuators, A*, 105, pp. 211- 224.
- [3] Y. Chen, S. Kang, W. Tuh, and T. Hsiao, 2004, "Experimental Investigation of Fluid Flow and Heat Transfer in Microchannels," *Tamkang Journal of Science and Engineering*, 7(1), pp. 11-16.
- [4] H.Y. Wu, P. Cheng, "An Experimental Study of Convective Heat Transfer in Silicon Microchannels with Different Surface Conditions," *Int. J. Heat Mass Transfer* 46 (14) (2003) 2547- 2556.
- [5] W. Qu, I. Mudawar, "Analysis of Three-Dimensional Heat Transfer in Microchannel Heat Sinks," *Int. J. Heat Mass Transfer* 45 (2002) 3973-3985.

- [6] A.G. Fedorov, R. Viskanta, "Three-dimensional Conjugate Heat Transfer in the Microchannel Heat Sink for Electronic Packaging," *Int. J. Heat Mass Transfer* 43 (3) (2000) 399-415.
- [7] Fedorov, R. Viskanta, "A Numerical Simulation of Conjugate Heat Transfer in an Electronic Package Formed by Embedded Discrete Heat Sources in Contact with a Porous Heat Sink," *ASME Journal of Electronic Packaging* 119 (1997) 8-16.
- [8] Weisberg, H.H. Bau, J.N. Zemel, "Analysis of Microchannels for Integrated Cooling," *Int. J. Heat Mass Transfer* 35 (1992) 2465-2474.
- [9] R.W. Knight, J.S. Goodling, D.J. Hall, "Optimal Thermal Design of Forced Convection Heat Sinks-Analytical," *ASME J. Electron Packaging*, No.113, pp.313-321, 1991.
- [10] R.W. Keyes, "Heat Transfer in Forced Convection through Fins," *IEEE Trans. Electron Dev.* ED-31 (1984) 1218-1221.
- [11] Bejan, A.M. Morega, "Optimal Arrays of Pin Fins and Plate Fins in Laminar Forced Convection," *ASME J. Heat Transfer* 115 (1993) 75-81.
- [12] D.Y. Lee, K. Vafai, "Comparative Analysis of Jet Impingement and Microchannel Cooling for High Heat Flux Applications," *Int. J. Heat Mass Transfer* 42 (1999) 1555-1568.
- [13] X.F. Peng, G.P. Peterson, "Convective Heat Transfer and Flow Friction for Water Flow in Microchannel Structures," *Int. J. Heat Mass Transfer* 39 (12) (1996) 2599-2608.
- [14] K. Kawano, K. Minakami, H. Iwasaki, M. Ishizuka, "Development of Micro Channels Heat Exchanging," in: R.A. Nelson Jr., L.W. Swanson, M.V.A. Bianchi, C. Camci (Eds.), *Application of Heat Transfer in Equipment, Systems, and Education*, HTD-Vol. 361-3/PID-Vol. 3, ASME, New York, 1998, pp. 173-180.
- [15] H.Y. Wu, P. Cheng, "Friction Factors in Smooth Trapezoidal Silicon Microchannels with Different Aspect Ratios," *Int. J. Heat Mass Transfer* 46 (14) (2003) 2519-2525.
- [16] P. Cheng, C.T. Hsu, A. Choudhury, "Forced Convection in the Entrance Region on a Packed Channel with Asymmetric Heating," *ASME Journal of Heat Transfer* 110 (1988) 946-954.
- [17] J.C.Y Koh, R. Colony, 1986, "Heat Transfer of Micro Structures for Integrated Circuits," *Int. Commun. Heat Mass Transfer*, 13, pp. 89-98.
- [18] C.L Tien, S.M. Kuo, 1987, "Analysis of Forced Convection in Microstructures for Electronic Systems Cooling," *Proc. Int. Symp. Cooling Technology for Electronic Equipment*, Honolulu, HI, August 31-September 2, pp. 217-226.
- [19] R.L. Webb, M. Zhang, "Heat Transfer and Friction in Small Diameter Channels," *Microscale Thermophysical Engineering* 2 (1998) 189-202.
- [20] E. Eckert, R. Drake, "Analysis of Heat and Mass Transfer," McGraw-Hill, New York, 1972.
- [21] J. Ferziger, M. Peric, "Computational Methods for Fluid Dynamics," Berlin: Springer-Verlag, 1996. ISBN 3-540-59434-5.
- [22] C.M. Rhie, W.L. Chow, "Numerical Study of the Turbulent Flow Past an Airfoil with Trailing Edge Separation," *AIAA Journal*, Vol. 21, November 1983, pp. 1525-1532.
- [23] B.R. Hutchinson, G.D. Raithby, "A Multigrid Method Based on the Additive Correction Strategy," *Numer. Heat Transfer* 9 (1986)511-537.
- [24] R.K. Shah, A.L. London, "Laminar Flow Forced Convection in Ducts," Academic Press, NY, 1978, pp. 78-283.

- [25] Bejan, "Convection Heat Transfer," first ed., John Wiley & Sons, New York, 1984.
- [26] S. Kakac, Y. Yener, "Convective Heat Transfer," second ed., CRC Press, Begell House, Boca Raton, 1995.
- [27] A.F. Mills, "Heat Transfer," second ed., Prentice Hall, Upper Saddle River, 1999.



## Heat Exchangers - Basics Design Applications

Edited by Dr. Jovan Mitrovic

ISBN 978-953-51-0278-6

Hard cover, 586 pages

**Publisher** InTech

**Published online** 09, March, 2012

**Published in print edition** March, 2012

Selecting and bringing together matter provided by specialists, this project offers comprehensive information on particular cases of heat exchangers. The selection was guided by actual and future demands of applied research and industry, mainly focusing on the efficient use and conversion energy in changing environment. Beside the questions of thermodynamic basics, the book addresses several important issues, such as conceptions, design, operations, fouling and cleaning of heat exchangers. It includes also storage of thermal energy and geothermal energy use, directly or by application of heat pumps. The contributions are thematically grouped in sections and the content of each section is introduced by summarising the main objectives of the encompassed chapters. The book is not necessarily intended to be an elementary source of the knowledge in the area it covers, but rather a mentor while pursuing detailed solutions of specific technical problems which face engineers and technicians engaged in research and development in the fields of heat transfer and heat exchangers.

### How to reference

In order to correctly reference this scholarly work, feel free to copy and paste the following:

Mohammad Hassan Saidi, Omid Asgari and Hadis Hemati (2012). Microchannel Simulation, Heat Exchangers - Basics Design Applications, Dr. Jovan Mitrovic (Ed.), ISBN: 978-953-51-0278-6, InTech, Available from: <http://www.intechopen.com/books/heat-exchangers-basics-design-applications/microchannel-simulation>

# INTECH

open science | open minds

### InTech Europe

University Campus STeP Ri  
Slavka Krautzeka 83/A  
51000 Rijeka, Croatia  
Phone: +385 (51) 770 447  
Fax: +385 (51) 686 166  
[www.intechopen.com](http://www.intechopen.com)

### InTech China

Unit 405, Office Block, Hotel Equatorial Shanghai  
No.65, Yan An Road (West), Shanghai, 200040, China  
中国上海市延安西路65号上海国际贵都大饭店办公楼405单元  
Phone: +86-21-62489820  
Fax: +86-21-62489821

© 2012 The Author(s). Licensee IntechOpen. This is an open access article distributed under the terms of the [Creative Commons Attribution 3.0 License](#), which permits unrestricted use, distribution, and reproduction in any medium, provided the original work is properly cited.